ADVANCED ELECTRONIC MATERIALS
www.advelectronicmat.de

Origin of Ferroelectric Phase Stabilization via the Clamping Effect in Ferroelectric Hafnium Zirconium Oxide Thin Films

*Shelby S. Fields, Truong Cai, Samantha T. Jaszewski, Alejandro Salanova, Takanori Mimura, Helge H. Heinrich, Michael David Henry, Kyle P. Kelley, Brian W. Sheldon, and Jon F. Ihlefeld**

The presence of the top electrode on hafnium oxide-based thin films during processing has been shown to drive an increase in the amount of metastable ferroelectric orthorhombic phase and polarization performance. This "Clamping Effect," also referred to as the Capping or Confinement Effect, is attributed to the mechanical stress and confinement from the top electrode layer. However, other contributions to orthorhombic phase stabilization have been experimentally reported, which may also be affected by the presence of a top electrode. In this study, it is shown that the presence of the top electrode during thermal processing results in larger tensile biaxial stress magnitudes and concomitant increases in ferroelectric phase fraction and polarization response, whereas film chemistry, microstructure, and crystallization temperature are not affected. Through etching experiments and measurement of stress evolution for each processing step, it is shown that the top electrode locally inhibits out-of-plane expansion in the HZO during crystallization, which prevents equilibrium monoclinic phase formation and stabilizes the orthorhombic phase. This study provides a mechanistic understanding of the clamping effect and orthorhombic phase formation in ferroelectric hafnium oxide-based thin films, which informs the future design of these materials to maximize ferroelectric phase purity and corresponding polarization behavior.

1. Introduction

HfO_2-based thin films have been the subject of extensive research and development for nonvolatile memory,[1–3] negative differential capacitance field-effect transistor,[4,5] nonlinear optic,[6] and energy harvesting[7,8] applications following the first reporting of their stable polarization hysteresis properties in thin films in 2011.[9] These properties have since been attributed to a metastable ferroelectric $Pca2_1$ orthorhombic phase,[9–11] which has been observed to have a coercive field of ≈1.1 MV cm^{-1}[12] and calculated to have a theoretical spontaneous polarization of ≈50 μC cm^{-2}.[10] This polar ferroelectric phase is stabilized relative to the bulk, room temperature linear dielectric $P2_1/c$ monoclinic and high-temperature, field-induced ferroelectric $P4_2/nmc$ tetragonal phases through processing to produce small grain sizes,[13,14] inclusion of a variety of dopants,[9,15–17] imparting of biaxial stress,[18,19] and incorporation of point defects.[20–22] Alloying with ZrO_2 ($Hf_{1-x}Zr_xO_2$, HZO), in particular, has been observed to yield a stable ferroelectric response through nearly the entire composition window ($0.0 < x < 0.8$).[7,17,23] The HZO material system is particularly attractive for device technologies owing to the scalability of the ferroelectric properties,[24] chemical compatibility of both HfO_2 and ZrO_2 with silicon,[25,26] and the existence of mature atomic layer deposition (ALD) processes in semiconductor fabrication facilities.

Since the first reports of ferroelectricity in HfO_2-based thin films, the presence of a capping layer, deposited on top of the

S. S. Fields, S. T. Jaszewski, A. Salanova, T. Mimura, H. H. Heinrich, J. F. Ihlefeld
Department of Materials Science and Engineering
University of Virginia
Charlottesville, VA 22904, USA
E-mail: jfi4n@virginia.edu

The ORCID identification number(s) for the author(s) of this article can be found under https://doi.org/10.1002/aelm.202200601.

DOI: 10.1002/aelm.202200601

T. Cai, B. W. Sheldon
Department of Engineering
Brown University
Providence, RI 02912, USA

M. D. Henry
Sandia National Laboratories
Albuquerque, NM 87185, USA

K. P. Kelley
Center for Nanophase Materials Sciences
Oak Ridge National Laboratory
Oak Ridge, TN 37381, USA

dielectric before annealing, has been observed to enhance the resultant measured polarization response and orthorhombic phase fractions.[9,27–29] Early investigations of the top electrode-dependent polarization behavior suggested that the mechanical clamping from the top electrode, typically a metallic binary nitride such as TiN or TaN,[22] was absolutely necessary to stabilize the orthorhombic phase.[19,27,30] Subsequent investigations have since demonstrated stable ferroelectric polarization in thin films annealed without a capping top electrode.[16,31,32] Regardless, superior polarization performance and greater orthorhombic phase fractions are obtained when HZO devices are processed with a top electrode in place,[33] with similar observations made for the Al and Y-doped HfO_2 thin film systems.[16,34] These results associate the improved polarization response with the suppression of the transformation from the high-temperature tetragonal phase to the room temperature monoclinic phase upon cooling from the crystallization temperature, producing the orthorhombic phase due to mechanical confinement instead.[30]

Early computational works predicted enhanced orthorhombic phase stability due to biaxial and hydrostatic compressive stresses owing to a volumetric constriction during transformation from the high-temperature tetragonal to the room-temperature monoclinic phases.[10,35] More recent computation studies, however, demonstrate that tensile strains are required to stabilize the ferroelectric phase[36] and this is supported by experiments showing increased orthorhombic phase fractions in film stacks possessing larger tensile stresses.[37] Additionally, experimental works have demonstrated that biaxial tensile stresses favor domain structures that orient the short, polar *c*-axis perpendicular to the film surface, resulting in higher measured polarizations.[18,19,38] Thus, in HfO_2-based thin film systems, the ultimate effect of the imparted stress is a combination of the stabilization of the orthorhombic phase relative to the tetragonal and monoclinic phases and the orientation of the resulting domain structure. In the context of the clamping effect larger polarizations and orthorhombic phase fractions due to the presence of the top electrode have been correlated with larger tensile biaxial stresses.[33,37] However, with the assumption that each of the films within a multilayer is uniform, well bonded, only elastically deforms, and is sufficiently thin, the thermal biaxial stresses of each should only be related to their respective coefficient of thermal expansion (CTE) mismatch with the employed substrate.[39,40] Therefore, the presence of the top electrode layer, if deposited with a similar thickness as the underlying HfO_2-based ferroelectric, should not directly affect the hafnia's post-processing biaxial stress state.

While biaxial stress imparted due to mechanical clamping is most commonly credited with impacting both the relative stability of the ferroelectric phase and the resulting domain structure within ferroelectric HZO thin films,[17,30,37] experimental works have also observed changes in grain size and microstructure associated with the presence of the top electrode.[41] Given that small grain sizes are widely observed to facilitate orthorhombic phase stabilization,[35] examination of composition and thickness-varied HZO devices has shown that grain size decreases and polarization increases as film thickness decreases below 20 nm.[42] Within this prior investigation, it was concluded that the presence of the top electrode did not influence the grain size of ≈9.1 nm thick HZO films; however, the effects of the top electrode presence during annealing on the grain size of the thicker films was not examined. A separate study, which made atomic force microscopy (AFM) measurements of 4 nm thick HfO_2 films, annealed with and without a TiN top electrode, reported that the presence of the top electrode resulted in smaller grain sizes and lower surface roughness. However, the annealing conditions selected in this referenced study, 400 °C in N_2 for 30 min, were widely different from the rapid thermal annealings typically utilized in processing of HfO_2-based ferroelectrics.[41] A more recent transmission electron backscatter diffraction investigation[43] of the phases present within a 10 nm thick HZO film between TiN electrodes revealed large contents of the orthorhombic phase throughout the 10–50 nm equivalent diameter grain size distribution, with measurable quantities of the monoclinic phase present in grains with equivalent diameters in excess of 25 nm, confirming the influence of grain size on the phase constitution.

Oxygen vacancy content has been theoretically predicted[13] and experimentally demonstrated[20,44] to be an important factor in orthorhombic phase stabilization and polarization response in HfO_2-based thin films. As such, deposition methods in which the ozone pulse length during ALD,[20,45] or oxygen flow during sputtering deposition,[44,46] have been optimized to yield large oxygen vacancy concentrations within the ferroelectric layers. Separate from ferroelectric layer deposition process optimization, interactions between these films and adjacent binary nitride electrodes have also been shown to affect the oxygen vacancy content and resultant polarization response.[47] Such electrode materials have been observed, using X-ray photoelectron spectroscopy (XPS), to form oxynitride interlayers[45,47,48] at the electrode/dielectric interfaces due to scavenging of oxygen from the dielectric layer during processing.[49] This oxygen scavenging phenomenon has been shown to affect the defect content within the ferroelectric layer, and the resulting phase constitution and polarization magnitude.[47] Thus, while the orthorhombic phase stabilization from the capping layer is typically attributed to imparted biaxial stress, such a process cannot be explained by classical multilayer thin film mechanics as discussed above, and chemical and microstructural interactions between the top electrode layer and the HfO_2-based ferroelectric present potential additional contributions to this effect.

In this study, the chemical and physical interactions between the TaN top electrode and 20 nm-thick ferroelectric HZO are investigated electrically and structurally. The phases present within the HZO and their post-processing biaxial stresses are characterized through area detector X-ray diffraction (XRD) measurements and $\sin^2(\psi)$ analyses. These biaxial stress values are compared with wafer flexure stress measurements made ex situ after each processing step and in situ during annealing. High-temperature XRD (HTXRD) and wafer flexure measurements are used to investigate how the biaxial stress evolves during the crystallization of these HZO ferroelectrics. Separately, the effects of the top electrode on the resulting film densification, defect densities, and grain morphology within the processed devices are examined through X-ray reflectivity (XRR), leakage current measurements, transmission electron microscopy (TEM), energy dispersive spectroscopy (EDS), and analysis of scanning electron microscopy (SEM) micrographs. Through the removal of top electrodes of fully processed devices, the important role of this layer on the stress state and phase within the HZO is revealed.

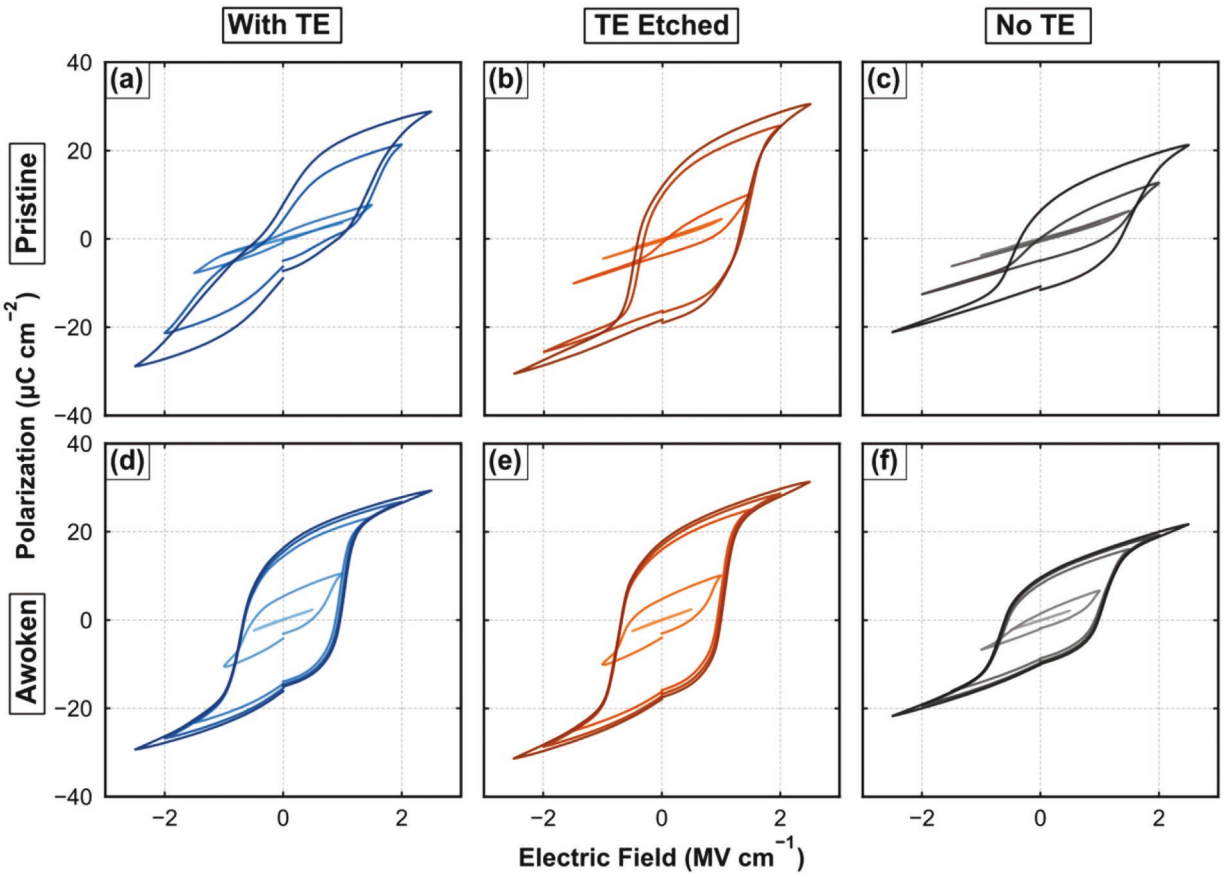

Figure 1. Nested $P(E)$ responses measured on pristine a) With-TE, b) TE-Etched, and c) No-TE devices and awoken d) With-TE, e) TE-Etched, and f) No-TE devices.

2. Results and Discussion

2.1. Comparison of Electrical Properties of Prepared Devices

To arrive at an understanding of the clamping effect in ferroelectric HZO thin films, three sample types were prepared: 100 nm TaN/20 nm HZO/20 nm TaN (referred to as "With-TE"), 100 nm TaN/20 nm HZO (referred to as "No-TE"), and 100 nm TaN/20 nm HZO/20 nm TaN stacks that had the 20 nm thick TaN top electrode layer removed via an SC-1 etch following thermal processing (referred to as "TE-Etched"). 280 μm thick, 50.8 mm diameter (001)-oriented silicon wafers with native oxides were employed as substrates. The TaN layers were all prepared by sputtering, and the HZO layers by ALD. The composition of the HZO layers was $Hf_{0.37}Zr_{0.63}O_2$. Unless otherwise stated, all thermal processes were conducted with a rapid thermal annealer to a temperature of 600 °C for 30 s in a nitrogen ambient. The With-TE and TE-Etched samples received a processing that is typically referred to as "post-metallization annealing" in the literature, whereas the No-TE sample received processing that is typically referred to as "post-deposition annealing." All samples were further processed to obtain identical TaN/HZO/TaN/Pt devices with discreet contact areas (100 to 500 μm in diameter) to perform comparable electrical characterization procedures. All process details are available in the Experimental section.

Nested polarization-electric field ($P(E)$, hysteresis) loops measured on each pristine device are shown in **Figure 1**a–c and display a strong dependence of polarization responses on the presence of the top electrode. Devices annealed with top electrodes (With-TE, TE-Etched) both exhibit larger polarizations than the No-TE device, which is consistent with results reported by other investigators.[9,33] Regardless of the presence of the top electrode, all polarization responses show saturation, consistent with low leakage current contributions. Comparing both samples processed with top electrodes, the hysteresis loops measured on the With-TE device are more pinched than those measured on the TE-Etched sample, which suggests that it contains more tetragonal phase that exhibits a field-induced ferroelectric response. The remanent polarization values (P_r, extracted from positive up negative down (PUND) measurements) measured on each of these pristine devices confirm this trend: the lowest P_r of 8.8 μC cm^{-2} was measured on the No-TE device, whereas the highest P_r of 17.5 μC cm^{-2} was measured on the TE-Etched device and a P_r of 14.1 μC cm^{-2} was measured on the With-TE device that exhibited a pinched $P(E)$ behavior. Analogous $P(E)$ measurements performed after 5000 1 kHz, 2.0 MV cm^{-1} square waves, plotted in Figure 1d–f, show that all three devices experienced polarization wake-up. The awoken $P(E)$ responses of devices processed with top electrodes similarly reveal larger polarizations than the response of the sample prepared without one. However, in contrast to the measurement performed on the pristine device, the $P(E)$ response measured on the With-TE device is no longer pinched, and the responses measured on the awoken With-TE and TE-Etched devices are nearly identical. The identical

polarization responses are evidence that the films contain essentially equivalent amounts of the orthorhombic phase following wake-up, which occurs in HfO_2-based ferroelectrics via oxygen vacancy redistribution, resulting in domain depinning[50,51] and transformations from the tetragonal to the orthorhombic phase.[52,53]

First-order reversal curve (FORC) measurements, which have been utilized to characterize domain dynamics in HfO_2-based ferroelectrics,[54,55] were carried out to further examine the evolution of the switching behavior between the With-TE, TE-Etched, and No-TE devices. A description of the measurement procedure and FORC data corresponding to each pristine and awoken device can be found in Figure S1a–f (Supporting Information). These measurements, once again, show larger switching density responses for the samples processed with top electrodes and polarization wake-up following cycling. The switching peak in the pristine With-TE measurement spans 1.0 MV cm^{-1} in α, which is larger than the switching peak in the TE-Etched measurement, which spans 0.5 MV cm^{-1}. Separated switching peaks are evidence of multiple coercive fields, which is a characteristic of an antiferroelectric-like polarization response.[56] Thus, the diffuse switching peak in the With-TE FORC response supports that this film contains more tetragonal phase than the TE-Etched film in the pre-awoken state. Similar to the $P(E)$ responses measured following wake-up, the FORC responses of the With-TE and TE-Etched devices are nearly identical and larger than the switching density response measured on the No-TE device.

To further investigate differences in electrical properties between the samples, capacitance–voltage (CV) measurements were carried out on the pristine and awoken devices, as shown in **Figure 2**a,b, respectively. Relative permittivities measured on the pristine devices, shown in Figure 2a, support that all three films comprise predominantly the tetragonal and orthorhombic phases, as evidenced by the values being larger than the 15–24 magnitudes typically reported for HZO films with large monoclinic phase contents.[17,57,58] The With-TE permittivity magnitudes are larger than those measured on the TE-Etched and No-TE films, which is indicative of larger contents of the higher permittivity tetragonal phase.[52] Further, the inhomogeneous switching observed in $P(E)$ loop and FORC measurements due to the partially antiferroelectric-like polarization response in the pristine With-TE film is also displayed in the pinching present in the vicinity of the positive coercive field in its accompanying CV measurement. Analogous CV measurements made following field cycling, shown in Figure 2b, reveal a reduction in relative permittivity values, which is consistent with polarization wake-up.[52,53] Similar to what was observed in the $P(E)$ and FORC polarization measurements made following field cycling, the pinching of the CV response in the vicinity of the positive coercive field in the pristine With-TE sample does not persist following cycling. However, while the $P(E)$ and FORC responses of the With-TE and TE-Etched devices are virtually identical following wake-up, the relative permittivity values measured for the awoken With-TE film are higher by 1.5–3 than the values measured for the TE-Etched film. The lower relative permittivity in the TE-Etched film indicates that this film may contain a slightly greater amount of the lower permittivity monoclinic phase than the With-TE film.[52]

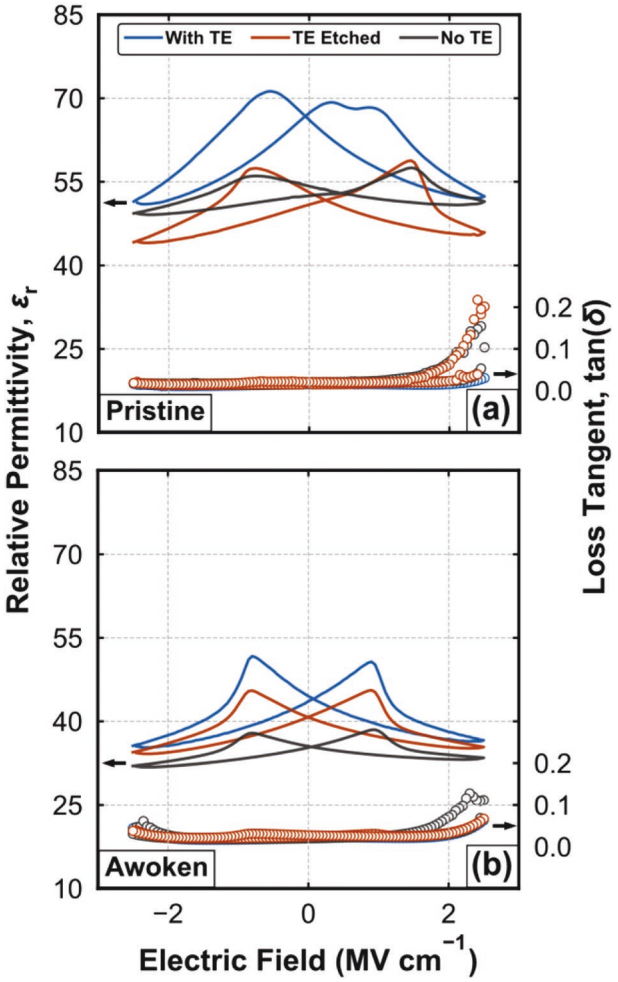

Figure 2. Relative permittivity (left axis, lines) and loss tangent (right axis, open points) versus electric field for a) pristine and b) awoken With-TE (blue), TE-Etched (orange), and c) No-TE (gray) films.

2.2. Analysis of Phase Constitutions

Grazing-Incidence X-ray diffraction (GIXRD) patterns measured on fully processed With-TE, TE-Etched, and No-TE devices, shown in **Figure 3**, reveal differences in phase constitutions in all three samples. The pattern measured on the No-TE film contains peaks at 28.5°, 30.7°, and 31.7° in 2θ corresponding to the $(\bar{1}11)$ monoclinic (m_1), superimposed (101) tetragonal and (111) orthorhombic (t + o), and (111) monoclinic (m_2) reflections, respectively. The pattern measured on the TE-Etched film exhibited a strong t + o peak, a weak m_2 peak, and a m_1 peak only slightly above the background level. The pattern measured on the With-TE film contained a strong t + o peak and a m_2 peak only slightly above the background level. Integrated intensities for each peak were calculated and compared to estimate the relative quantities of the t + o phase in each film using Equation (1):

$$f_{t+o} = \frac{I_{t+o}}{I_{t+o} + I_{m_1} + I_{m_2}} \quad (1)$$

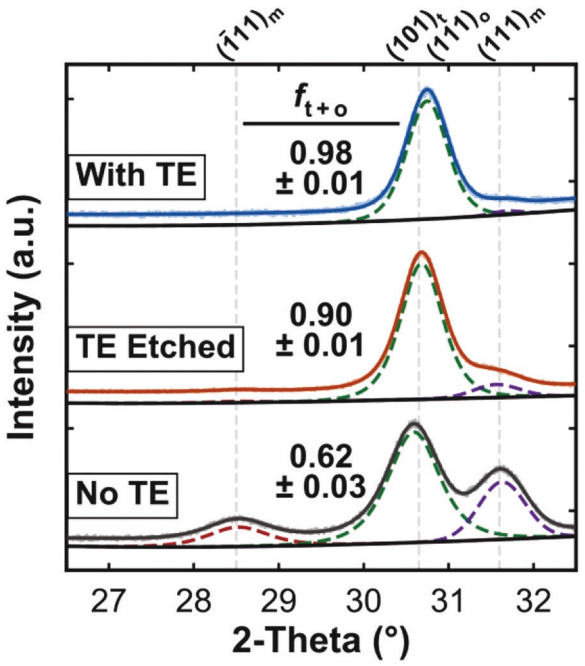

Figure 3. GIXRD patterns measured on the No-TE (gray), TE-Etched (orange), and With-TE (blue) films. The fits for each observed ($\bar{1}11$) monoclinic (red dotted line), t + o (green dotted line) and (111) monoclinic (purple dotted line) peak and fit background (black line) are offset below each corresponding pattern. The indexing for each observed peak is indicated by gray vertical dotted line and listed above the panel, and the calculated t + o fraction is indicted to the left of each corresponding pattern.

where I_{t+o}, I_{m_1}, and I_{m_2} are the integrated intensities of the t + o, m_1, and m_2 diffraction peaks, respectively, and f_{t+o} is the relative t + o phase fraction. Using this calculation, quantitative t + o phase fractions within each sample can be compared. These fractions were determined to be 0.98 ± 0.01, 0.90 ± 0.01, and 0.62 ± 0.03 for the With-TE, TE-Etched, and No-TE films, respectively. Thus, by comparison, the No-TE film contains less t + o phases than the With-TE and TE-Etched films, which supports the trends observed from polarization measurements. Moreover, the increase in m_1 and m_2 intensity between the With-TE and TE-Etched samples, and corresponding decrease in f_{t+o} is evidence that the top electrode removal process has increased the amount of monoclinic phase in the TE-Etched film. This increase in the amount of monoclinic phase due to etching would require a corresponding reduction in the amount of the orthorhombic and/or tetragonal phases in this film. The lower relative permittivities and reduction in hysteresis pinching observed when comparing data from the TE-Etched and With-TE films suggest that the monoclinic phase produced by removing the top electrode is, at least partially, due to a transformation from the tetragonal phase. Further, the identical polarizations measured on both samples following wake-up are indicative that both contain similar amounts of orthorhombic phase. However, changes in relative permittivity can be attributed to factors besides phase transformations, and the wake-up process is known to occur, in part, due to phase transformations from the tetragonal to the orthorhombic phase.[53] Therefore, while changes in relative permittivity and polarization behavior are consistent with a phase transformation mostly between the tetragonal and monoclinic phases, transformations between the orthorhombic and monoclinic phases cannot be completely dismissed.

The presence of more intense monoclinic reflections in the TE-Etched diffraction pattern, lower relative permittivity, and more homogeneous polarization switching in the pristine state compared to the pattern and responses measured on the With-TE film indicates that the removal of the top electrode affects the phase constitution in the HZO, possibly via a transformation from the tetragonal to the monoclinic phases. Given that the SC-1 process involves exposure of the film surface to an oxidizing $NH_4OH/HOOH/H_2O$ solution at 60 °C and that the phase constitution in HfO_2-based thin films is sensitive to oxygen content,[44] it is possible that the top electrode removal affected the HZO chemistry. Moreover, the large oxygen diffusivities in HfO_2[59] and ZrO_2[60] produce diffusion lengths for oxygen of 10s of nm at etch time and temperature, meaning that the SC-1 procedure could affect the chemistry of the entire film. To examine if the etch was responsible for changing the chemistry of the TE-Etched film, the sample was re-exposed to the SC-1 procedure identical to that utilized to remove the top electrode. The GIXRD patterns measured on the original TE-Etched and re-exposed TE-Etched (Re-exposed) films are compared in Figure S2 (Supporting Information) and reveal no difference in phase constitution. The relative t + o phase fraction for the re-exposed film was calculated to be 0.89 ± 0.01, which is identical to the fraction calculated for the original TE-Etched film. Thus, the extended exposure of the surface of the HZO to the oxidative solution does not appear to be responsible for the change in phase.

For a further investigation of the effects of top electrode removal on the phase constitution in the HZO layers, the With-TE samples were also processed using a low-power inductively coupled plasma reactive ion etch (ICP-RIE) to partially and fully remove the top TaN layer. The ICP-RIE process presents different oxidative conditions than the SC-1 wet etch procedure and is capable of selectively and partially removing the 20 nm top electrode layer. In addition, the low processing power and non-volatility between Hf, Zr, and SF_6 species mitigate potential damage or sputtering of the HZO surface. In **Figure 4**, the GIXRD patterns are measured on the original With-TE, a With-TE film that has had 15 nm of the 20 nm thick top TaN electrode removed via ICP-RIE (Partial RIE), and a With-TE film that has had the top TaN electrode removed completely via ICP-RIE (Full RIE) are compared. The relative t + o phase fractions calculated following the partial and full removal of the top electrode using the ICP-RIE process were 0.94 ± 0.01 and 0.88 ± 0.01, respectively. The fraction calculated for the Full RIE sample is identical to both the TE-Etched and Re-exposed films, and the fraction calculated for the Partial RIE film falls between the With-TE and fully etched films. These different etch procedures indicate that the increase in monoclinic phase fraction occurring during the removal of the top electrode is not related to a change in oxygen content in the HZO and is, therefore, related to a change in the mechanical boundary conditions.

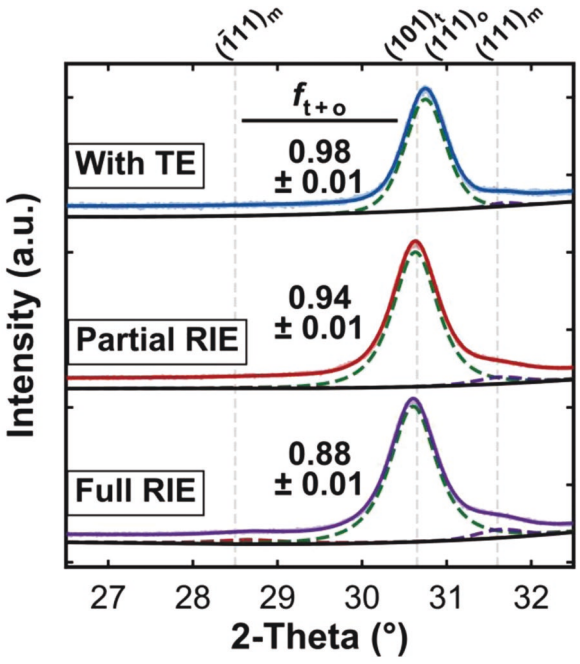

Figure 4. GIXRD patterns measured on the With-TE (blue), partial RIE (red), and full RIE (purple) films. The fits for each observed $(\bar{1}11)$ monoclinic (red dotted line), t + o (green dotted line), and (111) monoclinic (purple dotted line) peak and fit background (black line) are offset below each corresponding pattern. The indexing for each observed peak is indicated by gray vertical dotted line and listed above the panel, and the calculated t + o phase fraction is indicted to the left of each corresponding pattern.

2.3. Comparison of Chemical Properties of Prepared Devices

While changes in oxygen content between the With-TE and TE-Etched samples do not appear to be driving the transformation to the monoclinic phase resulting from electrode etching, such variations related to processing with or without the top electrode could be contributing to the clamping effect. To examine differences in defect concentration and oxygen content due to the presence of the top electrode during processing, leakage current, and scanning transmission electron microscopy-energy dispersive X-ray spectroscopy (STEM-EDS) measurements were carried out. While direct examination of defect concentrations in HfO_2-based thin films is experimentally difficult, leakage current measurements have been employed to provide an estimation of these quantities.[20,47] Leakage current in ferroelectric HfO_2-based thin films has been attributed to the presence of point defects, such as oxygen vacancies[20,21] or trapped electrons,[58,61] which enable the transport of electrons via trap-assisted tunneling where the point defects act as traps.[62,63] Accordingly, larger leakage currents are indicative of greater defect concentrations.[20] Leakage current measurements of pristine and awoken With-TE, TE-Etched, and No-TE devices, shown in Figure S3a,b (Supporting Information), reveal similar leakage current profiles following cycling for all three devices. In the pristine state, different asymmetries are present in the data. These are likely related to the different processing conditions and asymmetric interfaces and prevent direct comparisons. Following field cycling, the leakage current profiles are more similarly asymmetric and are of identical magnitudes. While the profile asymmetries prevent fitting the data to trap assisted tunneling models,[20,62,63] qualitatively, the similar current magnitudes indicate that the presence of the top electrode and its removal does not appear to have a significant impact on the defect concentrations in the samples.

The similar defect concentrations, particularly between the With-TE and No-TE samples, indicate that the HZO films have similar oxygen contents regardless of whether the top electrode was in place during processing. To further examine the stoichiometry of these two samples, STEM-EDS profiles were measured across the film thicknesses, as shown in **Figure 5**a–d. High-angle annular dark field (HAADF) micrographs collected on the With-TE and No-TE films, shown in Figure 5a,b, were utilized to confirm HZO film thicknesses of 20 nm and reveal the presence of ≈1 nm TaO_xN_y interlayers separating the HZO layers and TaN electrodes, which form due to oxygen scavenging during thermal processing.[22,47,48] EDS profiles, shown in Figure 5c,d for the With-TE and No-TE samples, respectively, were measured with a signal summation over a width of 10 nm across film thicknesses. By averaging the Hf, Zr, and O atomic fractions within the middle 5 nm of each film, compositions of $Hf_{0.43\pm0.07}Zr_{0.56\pm0.06}O_{1.34\pm0.05}$ and $Hf_{0.40\pm0.03}Zr_{0.60\pm0.06}O_{1.25\pm0.07}$ were determined for the With-TE and No-TE samples, respectively. While EDS measurements are challenged to reliably quantify oxygen content without a suitable standard, the Hf:Zr ratio for both of the samples is the same within error, which would be expected given that they were prepared with identical deposition conditions, and both films are oxygen deficient, which is consistent with other studies of the oxygen content in HfO_2-based thin films with large contents of the orthorhombic phase.[20,44] Therefore, the film defect concentrations and stoichiometries are similar or identical regardless of the presence of the top electrode during processing insofar as these characteristics can be compared using leakage current measurements and STEM-EDS.

2.4. Effects of Top Electrode on Film Microstructure

While the presence of the top electrode was not observed to affect the defect concentration and oxygen content of the processed films, it may affect the HZO grain sizes.[41] Such a change could affect the phase constitution given the lower surface energy of the orthorhombic phase compared to the monoclinic,[13,35,42] and thus be a driving mechanism of the clamping effect. To examine if the presence of the top electrode during thermal processing affects the HZO grain sizes of processed devices, grain watershed and lineal intercept analyses were carried out on atomic force microscopy (AFM) and scanning electron microscopy (SEM) data, respectively, captured on the TE-Etched and No-TE films. According to watershed analysis of AFM topography scans captured on these samples, shown in **Figure 6**a–d, the TE-Etched and No-TE films exhibited similar median grain equivalent diameters of 25.3 ± 4.5 nm and 25.8 ± 4.6 nm, respectively. Plan-view scanning electron micrographs of the TE-Etched and No-TE films, shown in Figure S4 (Supporting Information) and analyzed using the ASTM E112 grain size measurement procedure,[64] also reveal similar grain

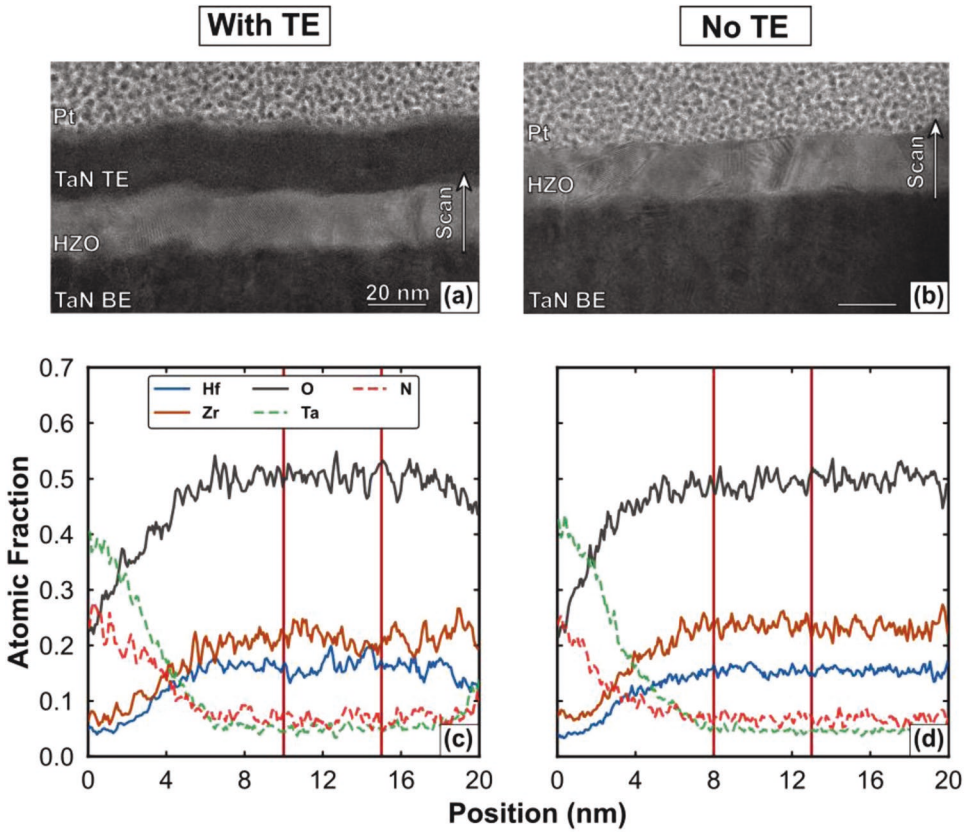

Figure 5. HAADF micrographs measured on the a) With-TE and b) No-TE films. The layer materials are indicated on the left of each micrograph, and the scale bars and scan directions are provided on the right. EDS compositions measured for the Hf (blue line), Zr (red line), O (gray line), Ta (green dotted line), and N (red dotted line) species across the c) With-TE and d) No-TE films. The regions between the solid vertical red lines in plots (c) and (d) were averaged to calculate $Hf_xZr_yO_z$ compositions for the With-TE and No-TE films, respectively.

equivalent diameters of 23 ± 1 and 22 ± 1 nm, respectively. Therefore, analysis of both AFM and SEM data reveals identical equivalent grain diameters, regardless of the presence of the top electrode during annealing. In tandem, inspection of STEM micrographs measured on both of these samples, shown in Figure 5a,b, reveals columnar structures and identical thicknesses (20 nm thick), supporting that plan-view measurements present valid estimations for grain sizes. Based on the small variance between the two grain sizes, differences in film phase or polarization related to size effects would not be anticipated.[13,43]

Separate from GIXRD of processed samples, high-temperature X-ray diffraction (HTXRD) patterns were collected on With-TE and No-TE samples to assess the effects of the presence of the top electrode on film crystallization temperature and phase formation. A difference in crystallization temperature dependent on the top electrode presence could contribute to the clamping effect, given that the monoclinic and tetragonal/orthorhombic phases have been reported to crystallize under different thermal budgets.[65] Therefore, if the top electrode reduced the crystallization temperature, larger tetragonal and orthorhombic phase compositions would be facilitated. Shown in **Figure 7**a,b are HTXRD measurements of the With-TE and No-TE samples. In both patterns, crystallization of the t + o phases was observed to begin at 390 °C, regardless of top electrode presence. While the With-TE film exhibited diffracted intensity corresponding to only the t + o reflection, peaks corresponding to the monoclinic phase were observed starting at 400 °C in the No-TE film. Intensity slightly above the background level is observed in the m_2 peak position in the patterns measured on the With-TE film beginning at 590 °C, which is consistent with the room-temperature GIXRD pattern measured following processing. This increase in m_2 intensity also coincides with a shift in the position of the t + o peak to a lower 2θ angle, which has been observed by other research groups.[65] Based upon a comparison of these two measurements, crystallization temperatures are unaffected by the presence of the top electrode in the HZO films, whereas the nucleating phases are different.

Given that crystallization of HZO films from amorphous states occurs with a concomitant increase in film density,[57] and that the difference in unit cell volumes contributes to the free energy differences between the phases,[10] fitting of X-ray reflectivity patterns measured on TE-Etched, No-TE, and amorphous films was undertaken to determine if the degree of densification during annealing varied due to the presence of the top electrode. The patterns and associated fits, shown in Figure S5 (Supporting Information), reveal HZO densification of +4.2% regardless of the presence of the top electrode. Before annealing, the amorphous HZO film had a density of 7.05 ± 0.02 g cm^{-3}. Identical densities of

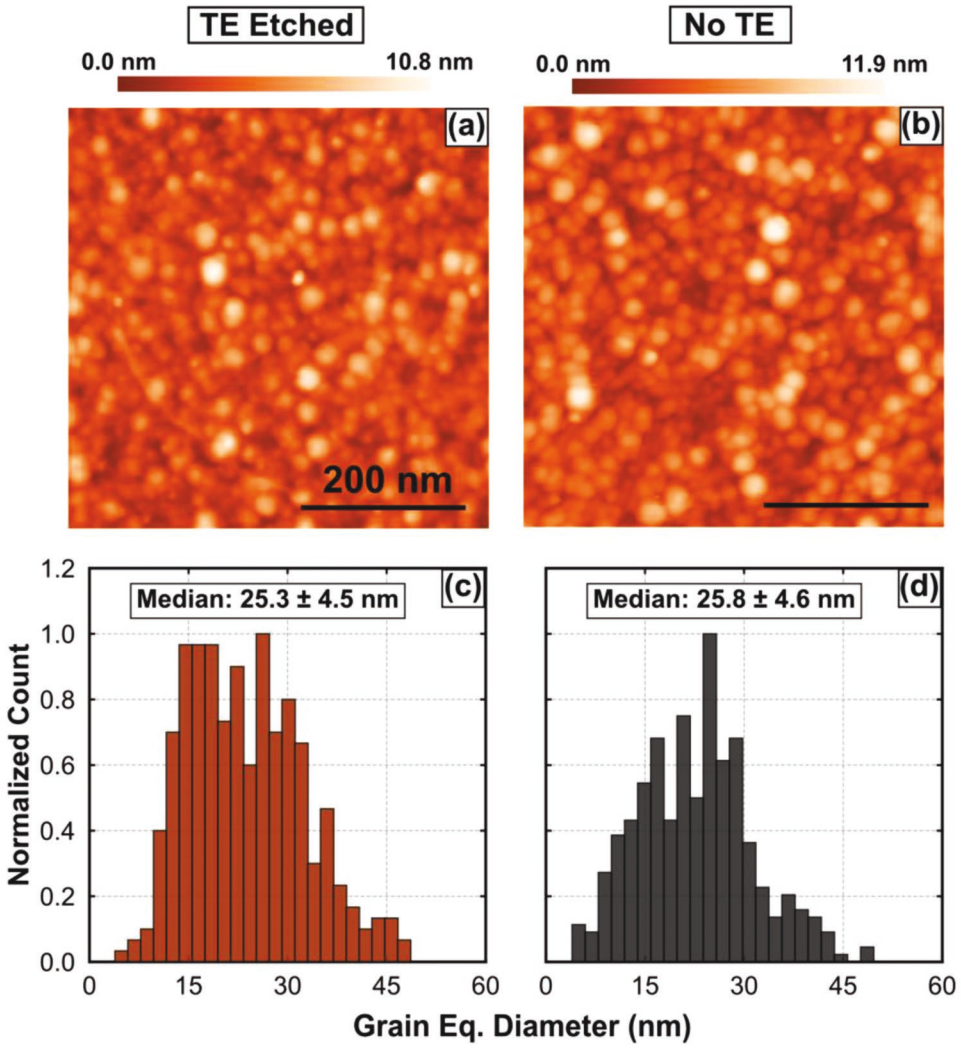

Figure 6. AFM topography scans measured on the a) TE-Etched and b) No-TE films. Results of watershed analysis completed on c) TE-Etched and d) No-TE AFM micrographs. The median grain equivalent diameters are identified above each analysis result.

7.35 ± 0.02 g cm^{-3} were fit for both the TE-Etched and No-TE samples following their processing. This densification coincided with a decrease in HZO thickness from 20.4 ± 0.1 nm for the amorphous film, to 19.8 ± 0.1 nm for both of the crystallized films. It should be noted that a densification of +2.0% was also observed in the TaN bottom electrode by separately rapid thermal annealing a 100 nm thick TaN layer on a silicon substrate, with the measured pattern and associated fit shown in Figure S6 (Supporting Information). This HZO and TaN densification suggest that the films should be in a tensile stress state, owing to clamping to a rigid single crystal substrate following their thermal processing; however, it does not clearly show that the presence of the top electrode affects the degree to which the films densify.

2.5. Quantification of Biaxial Stresses

While samples processed with and without top electrodes appear essentially identical when examined using chemical, microstructural, crystallization temperature, and densification measurements, they clearly possess different crystalline phase constitutions, relative permittivities, and polarization responses. It is evident, based on densification measurements, that the samples should be in states of tensile stress following processing, which has been shown to affect the orthorhombic phase stabilization and resulting domain structure.[10,18,66] To examine the amount of stress present within the HZO layers following processing due to both the presence and etched removal of the top electrode, $\sin^2(\psi)$ analyses were carried out on area detector diffraction patterns collected on each device structure.[57] The resulting changes in d-spacings with out-of-plane (ψ) angle and calculated biaxial stresses for each of the devices are shown in **Figure 8**a–c, with the collected area detector frames and unwarped patterns provided in Figure S7a–f (Supporting Information). With the assumption of uniform biaxial stresses in a randomly-oriented, isotropic linear elastic solid, fitting of the variation in d-spacing with ψ angle can be utilized to calculate the biaxial stress following processing using Equations (2) and (3):[67]

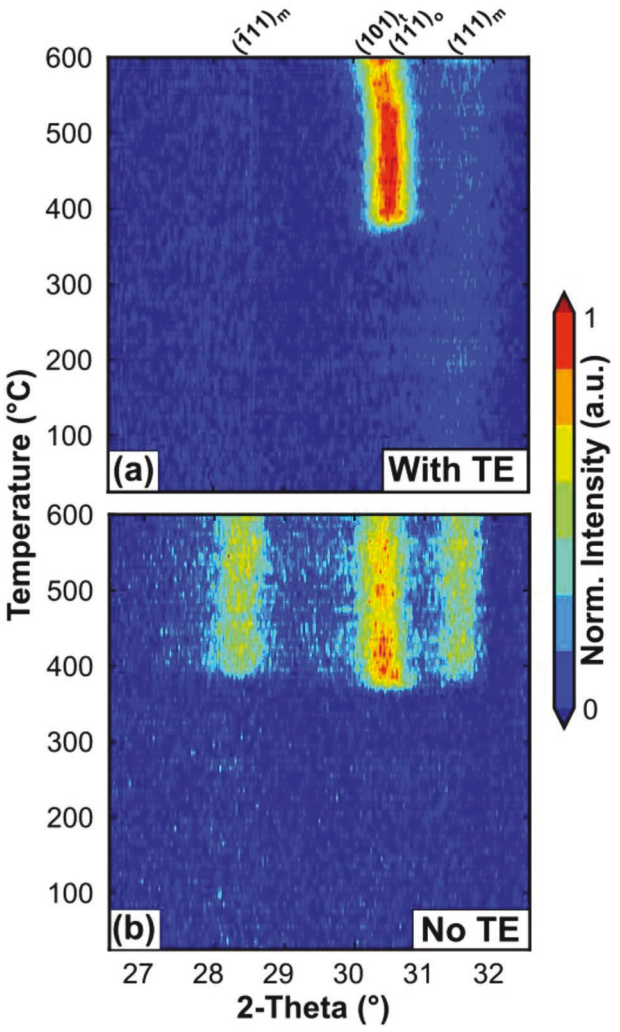

Figure 7. HTXRD patterns collected on a) With-TE and b) No-TE samples. Indexing for each of the observed peaks is indicated above the plots, and the colors corresponding to the normalized intensities are provided to the right.

$$\varepsilon_{\psi} = \frac{1+\nu}{E}\sigma_{\parallel}\sin^2(\psi) - \frac{2\nu}{E}\sigma_{\parallel} \tag{2}$$

$$\varepsilon_{\psi} = \frac{d_{\psi} - d_0}{d_0} \tag{3}$$

where d_{ψ} is the d-spacing at each ψ angle, ν is the Poisson's ratio of orthorhombic HZO (assumed to be 0.29[68–70] for this analysis), E is Young's modulus of orthorhombic HZO (assumed to be 209 ± 6 GPa for the With-TE and TE-Etched samples and 202 ± 6 GPa for the No-TE sample[57]), $\sigma_{\parallel}$ is the biaxial stress, and d_0 is stress-free d-spacing of orthorhombic HZO, which is calculated to occur at ψ angles at which Equation (4) is fulfilled:[67]

$$\sin\left(\psi^*\right) = \sqrt{\frac{2\nu}{1+\nu}} \tag{4}$$

The slopes of the linear fits of the changes in d-spacing with ψ angle were all found to be positive, which is indicative that all three samples are under tensile biaxial stress following processing and agree with the densification behavior observed using XRR. In tandem, the normalized integrated intensities of the t + o diffraction peaks were found to be essentially invariant with ψ angle, which is evidence that the films do not have a preferred orientation, validating the assumption of isotropic solids. The calculated tensile biaxial stress magnitudes were found to be between approximately 2 and 4 GPa, which is consistent with other similar investigations of HfO_2-based thin films with binary nitride electrodes.[38,47,57] When the HZO was processed without a top electrode, the resulting biaxial stress was calculated to be 2.10 ± 0.19 GPa, whereas when the film was annealed with a top electrode in place, the resulting biaxial stress was calculated to be 3.56 ± 0.18 GPa. Thus, the biaxial stress in the HZO resultant from the 'clamping effect' for these films is 1.46 ± 0.26 GPa (+73%). The TE-Etched film was calculated to have a biaxial stress of 2.74 ± 0.17 GPa following annealing and etching, indicating that the etching process decreased the amount of tensile biaxial stress in the HZO by 0.82 ± 0.25 GPa. Both the With-TE and TE-Etched samples exhibited larger tensile biaxial stresses and larger polarizations than the No-TE film following processing. The dissimilar stresses dependent on the top electrode presence highlight clear differences in these samples to accompany their different phase constitutions and polarization behaviors.

While diffraction measurements allow for the quantification of stress within the HZO layers due to the clamping effect and reveal clear differences in biaxial stress that accompany processing HZO thin films with and without a top electrode in place, they cannot quantify changes in stress that occur throughout the processing of the film stack. As a further examination of the evolution in biaxial stress with preparation of each sample, wafer flexure measurements following each film deposition, after annealing, and after etching were carried out. Example height profiles for all three samples, measured throughout processing, are shown in Figure S8a–c (Supporting Information). Each height profile was fit with a second degree polynomial, which was then utilized in Equation (5) to calculate a wafer radius of curvature following each processing step. Then, using radii of curvature fit before and after each step, the resultant biaxial stresses were obtained using the Stoney equation (Equation 6):[40]

$$R_{F,0} = \frac{\left[1+\gamma'(x)_{F,0}^2\right]^{\frac{3}{2}}}{\left|\gamma''(x)_{F,0}\right|} \tag{5}$$

$$\sigma_{\parallel} h_f = \frac{E_s h_s^2}{6(1-\nu_s)}\left(\frac{1}{R_F} - \frac{1}{R_0}\right) \tag{6}$$

where $R_{F,0}$ is the radius of curvature of the silicon substrate before (0) or following (F) the process step, $\gamma'(x)$ and $\gamma''(x)$ are the first and second derivatives of the polynomial height profile fit, respectively, $\sigma_{\parallel}$ is the biaxial stress resultant from the process step, h_f is the film thickness, in the case of deposition and etching steps, or total film stack thickness, in the case of the annealing steps, E_s is the elastic modulus of the silicon substrate (130 GPa[71]), h_s is the substrate thickness (280 µm), and ν_s is Poisson's ratio of the silicon substrate (0.28[71]). For these

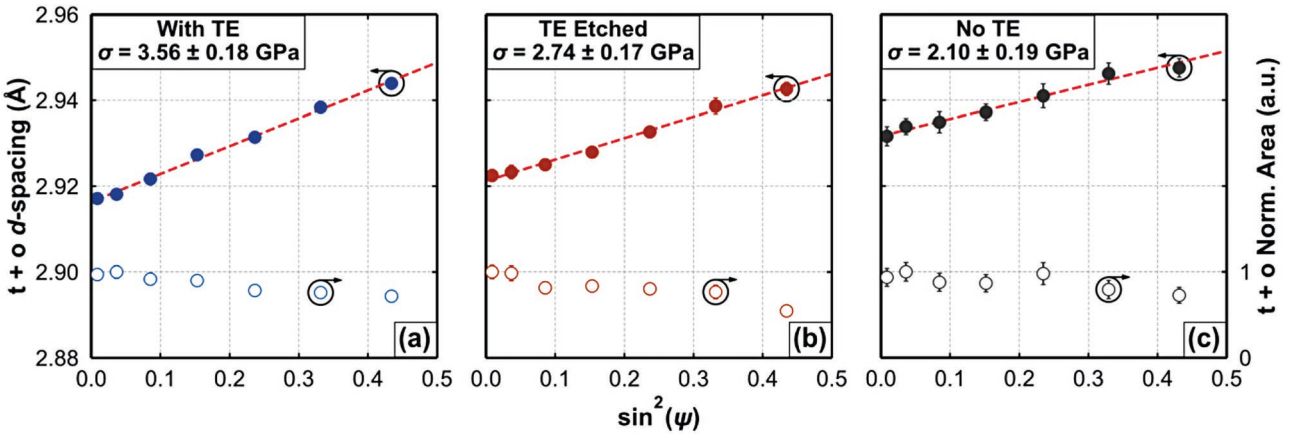

Figure 8. Change in t + o *d*-spacing (closed points, left axis) and t + o normalized area (open points, right axis) with ψ angle relative to film normal fit from area detector XRD patterns measured on a) With-TE, b) TE-Etched, and c) No-TE films. The linear fits (red dotted lines) plotted through the *d*-spacing data were utilized to calculate the biaxial stress following processing.

analyses, 95% confidence intervals of ±8 Pa m were determined through measurement of 16 separate 100 nm-thick TaN layers deposited directly on silicon.

The stress-thickness products ($\sigma_{\|} \times h_f$) measured following each processing step are detailed in **Figure 9**a–c for each device structure. The final film stacks were found to be strongly tensile following complete processing, in agreement with $\sin^2(\psi)$ analyses of the HZO and XRR densification analyses. Initial DC sputter deposition of the 100 nm thick TaN bottom electrode was measured to result in a stress-thickness product of −55 ± 8 Pa m in each sample. Next, plasma-enhanced atomic layer deposition (PEALD) of the 20 nm thick HZO layer led to a stress-thickness product of 40 ± 8 Pa m in the silicon substrates. DC sputter deposition of the 20 nm-thick top electrodes on the With-TE and TE-Etched samples resulted in a change in stress-thickness product of −12 ± 8 Pa m. Following depositions, rapid thermal annealing of the No-TE device was observed to result in a stress-thickness product increase of 93 ± 8 Pa m, whereas annealing the With-TE and TE-Etched devices resulted in an increase of 141 ± 8 Pa m. Thus, an additional 48 ± 8 Pa m (+51 ± 8%) of stress-thickness increase was observed for films processed with a top electrode layer. Further, etching of the top electrode following thermal processing resulted in a change in stress-thickness product of −14 ± 8 Pa m. By comparison, wafer flexure measurements and $\sin^2(\psi)$ analyses of the With-TE and No-TE samples predict stress-thickness product increases due to annealing that are similar, but outside of error, 48 ± 8 Pa m and 29.2 ± 6.0 Pa m, respectively, due to the clamping effect.

Differences between these two reported stress-thickness product changes due to the clamping effect may be related to the competing thermal expansion, mismatch, densification, and HZO crystallization contributions to the final flexure of the silicon substrate. As a further examination of the changes in wafer flexure produced by the annealing process, temperature-resolved wafer flexure measurements were carried out on the With-TE and No-TE film stacks using a multibeam optical stress

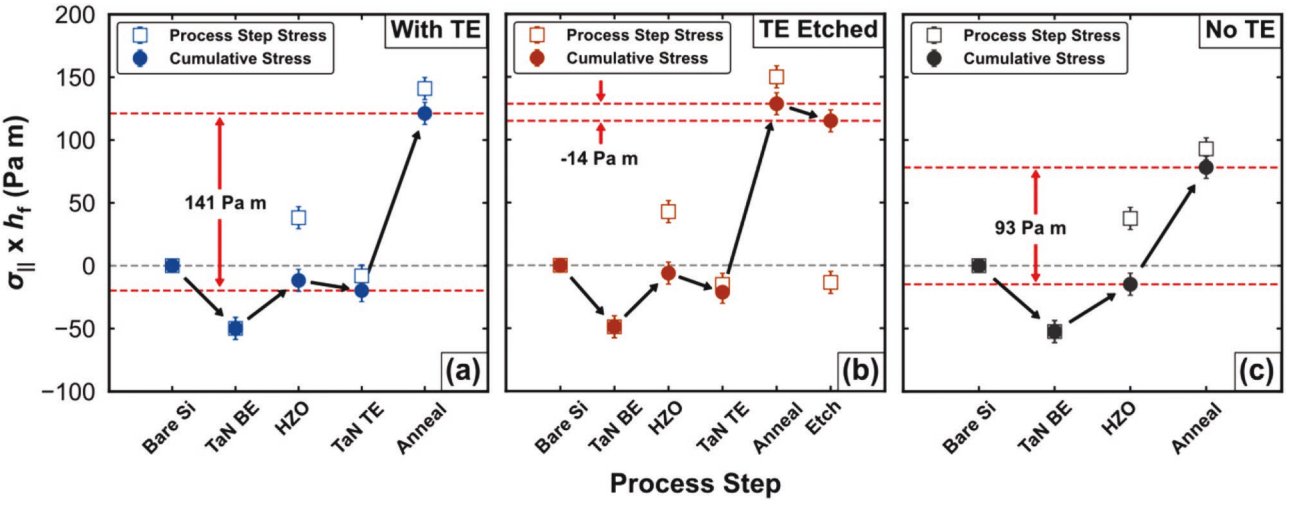

Figure 9. Cumulative (closed points) and individual process (open points) stress-thickness products quantified via wafer flexure measurements made on a) With-TE, b) TE-Etched, and c) No-TE samples. The grey dashed line indicates the 0 stress-thickness level, whereas the red dashed lines and red arrows indicate the stress-thickness changes resultant from annealing with the top electrode, etching of the top electrode following annealing, and annealing without the top electrode in (a), (b), and (c), respectively.

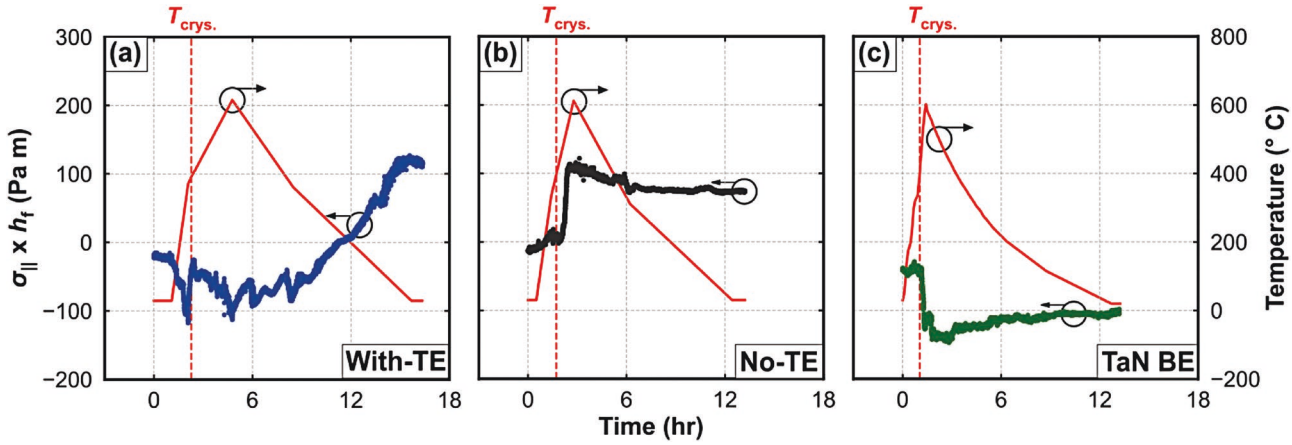

Figure 10. Wafer-flexure measured stress-thickness products (circles, left axis) and temperature profiles (red lines, right axis) from MOSS measurements made on a) With-TE, b) No-TE, and c) TaN bottom electrode film stacks.

sensor (MOSS) system, with results shown in **Figure 10**a–c. After an initial rest period of roughly 30 min, a temperature ramp rate identical to that utilized for HTXRD, 3 °C min^{-1}, was employed for these measurements so that the contributions from HZO crystallization to wafer flexure could be identified. The overall stress change of the With-TE sample, presented in Figure 10a, is approximately 135 Pa m, which is consistent with the 141 Pa m value reported by ex situ flexure measurements. Further, the data measured on the No-TE sample, shown in Figure 10b, indicates a final stress state of roughly 80 Pa m, which is similarly consistent with ex situ measurements of this stack following rapid thermal anneal.

The stress-thickness products obtained from the Stoney equation through MOSS measurement can be divided into contributions from the different layers, as described by Equation (7):

$$\sigma_{||} h_f = \sigma_{BE} h_{BE} + \sigma_{HZO} h_{HZO} + \sigma_{TE} h_{TE} \tag{7}$$

where σ_i and h_i are the i^{th} layer stress and thickness, respectively. This relationship assumes that films are ideal, having uniform properties and undergoing only elastic deformation. The stress in each layer is assumed to be influenced by the contributions detailed in Equation (8):

$$\sigma_i = \sigma_i^o + \Delta\sigma_i^P + \frac{E_i}{(1-\nu_i)}(\alpha_{Si} - \alpha_i)\Delta T \tag{8}$$

where σ_i^o is the intrinsic stress generated by the film deposition process, $\Delta\sigma_i^P$ is the stress change due to phase transformations, and the last term describes the thermal expansion mismatch. Here, α_i and α_{Si} are the coefficient of thermal expansion (CTE) values for the film material and silicon substrate, respectively. Although the CTE generally varies with temperature, these are approximated as constants in Equation (8) because values for the film materials are not currently known. Based on this description, the changes in stress observed in the experiments are due to either the CTE mismatch or $\Delta\sigma_i^P$. As shown in Figure 10c, the net compressive biaxial stress change during MOSS measurement of a single TaN BE layer is indicative of irreversible changes in the film structure. The cause of these changes is unclear, especially since densification of the TaN would be expected to produce tensile biaxial stress instead of the observed compression. It is possible that reactions with trace oxygen in the atmosphere during measurement lead to oxidation and modest volume expansion. Assuming that these changes occur primarily during heating, the cooling data below 300 °C could then be used to obtain an estimate of $\alpha_{TaN} \approx$ 8–10 ppm K^{-1}. Utilization of the TaN cooling data to calculate α_{HZO} using the data in Figure 10a,b was not possible given that the HZO layer was much thinner than the TaN bottom electrode. For all three films, the effect of thermal mismatch stress due to initial heating showed opposite trends compared to cooling, as expected. For example, in the No-TE data, the total thermal mismatch stress during heating (up to the onset of crystallization) was similar in magnitude to the cooling stress over the same temperature range. Note that these magnitudes are not necessarily identical because structural changes in the film can modify film CTE and elastic constants.

In both the With-TE and No-TE samples, the approximately 100 Pa m tensile biaxial stress increase at 390 °C can be attributed to crystalline phase formation within the HZO,[72] given that it is not observed during measurement of a bare TaN bottom electrode and coincides with the crystallization temperatures measured using HTXRD (Figure 7a,b). Tensile biaxial stress is consistent with the observation that crystallization leads to densification of the HZO layer (i.e., this shrinkage of the HZO leads to tensile stress because the film is constrained by the much thicker silicon substrate), which agrees with the ex situ XRR measurements made before and after rapid thermal processing, shown in Figure S5 (Supporting Information). After this initial tensile biaxial stress spike, the stress response of the With-TE and No-TE films differ. In the No-TE stack, the tensile biaxial stress increase is relatively brief, whereas the With-TE sample exhibits a more erratic stress response. These differences can be attributed to the presence of the top electrode and its influence on the HZO phases.

To further interpret the in situ curvature data, it is useful to make direct comparisons with the GIXRD data in Figure 3, where the final phase constitution of the With-TE and No-TE

samples are 98% and 62% t + o phase, respectively. In the With-TE sample, the complex stress-thickness behavior after the onset of crystallization can thus be interpreted as a combination of CTE effects and a competition of phase transformations of the metastable tetragonal and orthorhombic phases and the equilibrium monoclinic phase. This competition is influenced by the presence of the top electrode layer and will be discussed below. In contrast, the crystallization of the No-TE film stack exhibits a much simpler stress response in the same temperature range.

While the combination of HZO crystallization, thermal mismatches, and different densifications of all three layers prevent exact comparisons between thermal processing-related stresses and strains characterized using diffraction and wafer flexure, the etching process presents a simpler case. Diffraction analyses of this step using the t + o peak of the HZO showed a change in tensile biaxial stress of –0.82 ± 0.25 GPa, corresponding to a predicted stress-thickness product of –16.4 ± 5.0 Pa m in this layer, which agrees with direct examinations of this step using silicon wafer flexure, –14 ± 8 Pa m. Such agreement is expected given that the etching process occurs near room temperature and has a negligible contribution from densification changes. Given that this reduction in tensile biaxial stress coincides with a transformation of 8 ± 1% of the HZO film volume from the tetragonal and/or orthorhombic phases to the monoclinic phase, it can be taken as a reduction in the potential energy of the film. By utilizing the difference in biaxial stress in the HZO layer before and after top electrode removal, the change in the potential energy that coincides with this phase transformation, which is biaxial strain energy density in this case, can be calculated using Equation (9):

$$\Delta U_{\parallel} = \frac{\Delta \sigma_{\parallel}^2}{2E_{\parallel(\mathrm{HZO})}} \tag{9}$$

where $\Delta U_{\parallel}$ and $\Delta \sigma_{\parallel}$ are the change in biaxial strain energy density and biaxial stress due to the phase transformation, respectively, and $E_{\parallel(\mathrm{HZO})}$ is the biaxial modulus of HZO (assumed to be 278 ± 7 GPa for this analysis[57]). This calculation also assumes a uniform biaxial stress state and randomly oriented isotropic solid, as employed when utilizing Equations (2–4), and is reasonable given the invariance of the intensity of the t + o diffraction peak with ψ angle (Figure 8a,b). Using these assumptions and the average unit cell volume for the tetragonal and orthorhombic phases[35] (133.7 Å^3 per formula unit, F.U.$^{-1}$) results in a strain energy density change of –1.0 ± 0.5 meV F.U.$^{-1}$ during the transformation of 8 ± 1% of the volume of the film from the tetragonal and/or orthorhombic phases to the monoclinic phase. Based on these values, it can be extrapolated that a strain energy density change of –13.0 ± 6.0 meV F.U.$^{-1}$ would coincide with a complete transformation of the film to the monoclinic phase. For comparison, the total differences between the free energies of the orthorhombic and tetragonal structures and the monoclinic structure at room temperature, irrespective of the activation energy required for the transformation, have been calculated to be 25 and 70 meV F.U.$^{-1}$, respectively, by Materlik et al.[35]

2.6. Mechanism of the Clamping Effect in Ferroelectric HZO Devices

It is evident, based upon $\sin^2(\psi)$ and wafer flexure analyses, comparisons between film microstructures, and measurements of relative defect concentrations and stoichiometries, that the clamping effect in HfO_2-based thin films involves differences mainly in phase constitution and film mechanical stress. Through chemical and plasma etch removal of the top electrode, increases in the amount of monoclinic phase were observed, whereby full removal of the top electrode resulted in a decrease in f_{t+o} of 8 ± 1%. This increase in monoclinic phase fraction is accompanied by a decrease in tensile biaxial stress by 0.82 ± 0.25 GPa according to $\sin^2(\psi)$ analyses. Additional $\sin^2(\psi)$ analyses of samples that had the top electrode partially and fully removed via RIE, provided in Figure S9a,b (Supporting Information), revealed final biaxial stress states of 3.10 ± 0.30 and 3.09 ± 0.21 GPa, respectively, which represent decreases of 0.46 ± 0.35 and 0.47 ± 0.28 GPa, respectively. While the analyses are unable to differentiate between the biaxial stress states of the Partial and Full RIE samples due to the large errors, GIXRD patterns and $\sin^2(\psi)$ analyses demonstrate that the partial removal of the top electrode results in more minor reductions in tensile biaxial stress and transformations to the monoclinic phase than when the top electrode is completely removed.

The transformation from the tetragonal and/or orthorhombic phases to the monoclinic phase upon removal of the top electrode is indicative of the important role that the top electrode plays in the stabilization of the orthorhombic phase. If the bottom electrode, top electrode, and HZO films are idealized as homogeneous layers with uniform thicknesses and well-bonded planar interfaces, then the presence of the top electrode would have an insignificant effect on the biaxial stress in the HZO because the thin multilayer stack is constrained by the much thicker substrate.[39,40] Accordingly, the total $\sigma_{\parallel} h_f$ product in Equation (7) should be considered a membrane force that causes only a small amount of bending. The absence of the monoclinic phase in the With-TE sample can thus be explained by considering a localized mechanical constraint imposed by the top electrode on the out-of-plane displacement of the HZO. Considering that the tetragonal and orthorhombic phases have smaller molar volumes (higher densities) than the monoclinic phase,[35] crystallization of the equilibrium monoclinic phase counteracts in-plane tensile biaxial strains and also leads to a local out-of-plane expansion that is not constrained when thermal processing occurs without a top electrode in place. However, the top electrode mechanically constrains the out-of-plane expansion in the With-TE sample and thus restricts monoclinic phase formation. The erratic in situ stress response shown in Figure 10a suggests a process that is mechanically constrained from expansion in the out-of-plane axis, thus preventing the formation of the large molar volume monoclinic phase. Such a process would necessarily occur through expansion in directions that are not necessarily normal to the sample surface, but contain some normal projection, due to the random orientation and polycrystallinity of the HZO film. Such a local expansion in the HZO layer would require the top electrode to deform locally by expanding to accommodate the protrusion, thus increasing the local stress

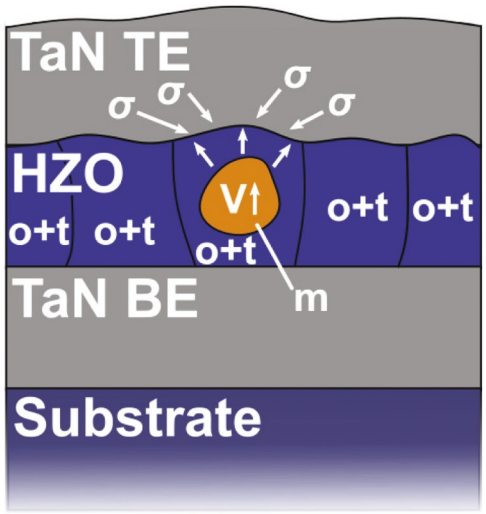

Figure 11. Diagram of clamping effect in ferroelectric HZO films with TaN electrodes. The local volumetric expansion associated with the formation of the monoclinic phase is hindered by the presence of the top electrode layer. Diagram not to scale.

in the top electrode layer. The energy penalty associated with additional stress in the electrode is too large, thus, any local formation of the monoclinic phase is hindered and the HZO remains in the tetragonal and/or orthorhombic phases. It is postulated that the erratic wafer flexure behavior observed is indicative of this competition of monoclinic phase embryos forming and local stress in the TaN top electrode preventing their growth into full nuclei, as diagrammed in **Figure 11**. Without the top electrode in place, local expansion of the HZO can occur as the lower free energy monoclinic phase forms. Therefore, the presence of the monoclinic phase in the No-TE and TE-Etched samples is because the HZO film is allowed to expand in the out-of-plane direction. This monoclinic phase formation drives the lower tensile biaxial stress states that are observed through ex situ $\sin^2(\psi)$ and wafer flexure-based stress analyses and in situ MOSS measurements rather than the lack of the electrode layer resulting in a reduced biaxial stress allowing for the formation of the monoclinic phase. Such a model is supported by other investigations of stress effects in HfO_2-based thin films, in which larger tensile biaxial stresses and orthorhombic phase fractions are reported for films with thicker, more mechanically constraining top electrode layers.[33] Moreover, in the context of the crystallization behavior of the With-TE sample characterized using HTXRD (Figure 7a), the increase in film-normal *d*-spacing of the t + o peak with the occurrence of m_2 intensity at 590 °C can thus be attributed to a reduction in tensile biaxial stress due to monoclinic phase formation.

3. Conclusion

To investigate the clamping effect in HZO thin films, the effects of processing of TaN/HZO/TaN metal/insulator/metal (MIM) samples with and without top electrodes have been examined using electrical, chemical, and structural measurements. It has been shown that processing HZO films with the top electrode in place produces more of the metastable ferroelectric orthorhombic phase than processing with only a bottom electrode layer, which results in films that are a mixture of the tetragonal, orthorhombic, and monoclinic phases. Comparisons between microstructural, leakage current, STEM-EDS, temperature-resolved XRD, and XRR measurements made on samples processed with and without top electrodes did not reveal discernable differences between oxygen content, grain sizes, crystallization temperatures, or densification behaviors dependent on the top electrode presence. Ex situ $\sin^2(\psi)$ and wafer-flexure-based stress analyses showed that processing samples with both electrodes in place produced tensile biaxial stresses that were higher than samples that were processed without the top electrode. The nature and mechanism of this difference in biaxial stress state were explored further through partial and full etching of the top electrode with wet etch and ICP-RIE procedures. It was determined that removal of the top electrode following processing results in a partial transformation of the HZO film to the monoclinic phase, which was accompanied by a reduction in the amount of tensile biaxial stress. This behavior was shown to not be related to oxidation from the etching procedures and persisted even if the electrode was only partially removed. Using this change in stress state and phase constitution, the activation energy barrier for the film to completely transform from the tetragonal and orthorhombic phases to the monoclinic phase was determined through calculations of changes in biaxial strain energy density. According to ideal thin film mechanics, however, contributions of the top electrode layer and its removal to the biaxial stress present within the HZO would be minor and well below the values observed in this study. Therefore, it was concluded that the phase transformation of the film to the larger molar volume monoclinic phase drives the reduction in tensile biaxial stress observed through etching experiments. Further temperature-resolved in situ wafer flexure measurements revealed erratic flexure behavior at high temperature when thermal processing occurred with a top electrode in place, which is consistent with an inhibition of out-of-plane expansion of the HZO film by local increases in tensile stress in the top electrode. Through these measurements, the following has been revealed about the clamping effect in HfO_2-based ferroelectric thin films:

1. The clamping effect in ferroelectric HfO_2-based thin films occurs due to an inhibition in local out-of-plane expansion of the film during crystallization by the top electrode.
2. The presence of the top electrode does not appear to measurably impact the densification behavior or crystallization temperature of the HZO layer.
3. Samples processed with top electrodes exhibit larger orthorhombic phase contents (+36 ± 3%) and tensile biaxial stress magnitudes (+70 ± 19%) than samples processed with only bottom electrodes.
4. Through removal of the top electrode, 8 ± 1% of the HZO film transforms to the monoclinic phase, driving a reduction in tensile biaxial stress of this layer by 23 ± 6%.
5. A transformation from a film in the tetragonal and orthorhombic phases to a film purely in the monoclinic phase is predicted to coincide with a strain energy density change of –13.0 ± 6.0 meV F.U.$^{-1}$.

4. Experimental Section

Sample Preparation Procedures: TaN/HZO/TaN metal-ferroelectric-metal devices were prepared on 50.8 mm diameter, 280 µm thick, (001)-oriented silicon substrates. The 100 nm thick planar TaN bottom electrodes were deposited via DC sputtering from a sintered TaN target with a power density of 3.3 W cm^{-2} under an argon background pressure of 5 mTorr in a 45° off-axis geometry. 20 nm thick HZO was next deposited using PEALD within an Oxford FlexAL II system at a temperature of 260 °C with tetrakis(ethylmethylamido)hafnium (TEMA Hf) and tetrakis(ethylmethylamido)zirconium (TEMA Zr) as HfO_2 and ZrO_2 precursors, respectively, and an oxygen plasma as the oxidant. Supercycles comprising five cycles of HfO_2 and five cycles of ZrO_2 were utilized for deposition, which resulted in a film composition of $Hf_{0.37}Zr_{0.63}O_2$, measured via X-ray photoelectron spectroscopy (XPS) using a PHI Versaprobe III XPS system. Next, a planar 20 nm thick TaN top electrode was deposited using the same conditions as the bottom electrode onto a subset of the HZO films. Samples prepared with and without a top electrode were then annealed at 600 °C within an Allwin21 AccuThermo 610 Rapid Thermal Processor for 30 s in a N_2 atmosphere. The temperature ramp and cooling rates were 50 and ≈2 °C s^{-1} for this procedure, respectively. Following annealing, a subset of samples processed with the top electrode received 50 nm-thick palladium contacts, deposited via DC sputtering through a shadow mask. After, all samples with top electrodes were subjected to an SC-1 bath (5:1:1 H_2O:30% H_2O_2 in H_2O:30% NH_4OH in H_2O) for 45 min at 60 °C to remove the blanket top electrode layer. For the samples on which palladium was deposited, the contacts acted as a hard mask, allowing for isolated TaN/HZO/TaN/Pd devices. On the samples that received only the blanket top electrode (which was etched following annealing) and samples that received no top electrode, 20 nm thick TaN top electrodes and 50 nm thick Pd contacts were deposited onto film surfaces through a shadow mask. Thus, in total, three sets of samples were prepared, 1) a set that was processed without a top electrode (referred to as "No-TE"), 2) a set that was processed with a top electrode (referred to as 'With-TE'), and 3) a set that was processed with a top electrode that was removed and replaced following annealing (referred to as "TE-Etched"). For additional etching experiments to isolate stress from chemical effects, top electrodes were partially and fully removed using a fluorine-based ICP-RIE procedure in a PlasmaTherm VersaLine inductively coupled plasma etcher. While etching, the pressure was held at 10 mTorr under 40 sccm of SF_6 and 10 sccm of argon gas flows. A 1200 W, 2 MHz coil power was utilized and a 13.56 MHz substrate bias of 30 W produced an etch rate of 27 nm min^{-1} for TaN with selectivity against HZO.

Electrical Characterization Procedures: Polarization-electric field ($P(E)$), positive up negative down (PUND), first-order reversal curve (FORC), and switching current loop measurements were made using a Radiant Technologies Precision LC II Tester. Nested $P(E)$ measurements were made with maximum applied fields between 1.0 and 2.5 MV cm^{-1} with a period of 1 ms. Nested PUND measurements were performed with maximum applied fields between 1.0 and 2.5 MV cm^{-1} with a 1 ms pulse width and a 1000 ms pulse delay. FORC measurements were made between ± 2.5 MV cm^{-1} with a step size of 0.1 MV cm^{-1}. Current loop measurements were made with a maximum applied field of 2.5 MV cm^{-1} with a 1 ms period. Capacitance-voltage (CV) measurements were carried out between ± 2.5 MV cm^{-1} with a 10 kHz, 50 mV AC oscillator using a Keysight E4980A LCR meter. Leakage currents were measured between ± 2.5 MV cm^{-1} using a Keysight B2901A Precision Source Measure Unit. All measurements were completed before and after 5000 2.0 MV cm^{-1} square wave field cycles that were applied at a frequency of 1 kHz.

Structural Characterization Procedures: GIXRD patterns were collected between 26° and 33° in 2θ using a Rigaku SmartLab diffractometer with Cu Kα radiation with the ω incident angle fixed at 0.7°. XRR patterns were collected between 0° and 5° in 2θ using the same instrument. Area detector X-ray diffraction patterns were collected using a Bruker D8 Venture diffractometer equipped with an Incoatec IµS 3.0 Cu Kα radiation source and a Photon III detector with ω incident angle fixed at 18°. For the area detector measurements, MgO powder was adhered to sample surfaces to act as a stress-free height alignment standard. The pyFAI fast azimuthal integration package[73] was utilized for area detector pattern unwarping, and LIPRAS[74] peak fitting software was utilized to fit Pearson VII shapes to all area detector line intensity profile and GIXRD patterns. XRR patterns were fit using GSAS-II software.[75] HTXRD measurements were collected in a Bragg-Brentano geometry between 25–600 °C and 26–33° in 2θ with 10 °C steps and a continuous 3 °C min^{-1} temperature ramp using a Malvern Panalytical Empyrean diffractometer using Cu Kα radiation, a GaliPIX detector, and an Anton Parr HTK 1200N High-Temperature Oven-Chamber. Wafer flexure measurements were completed following each processing step utilizing a Bruker DektakXT stylus profilometer. Scanning electron microscopy (SEM) measurements were performed with and transmission electron microscopy (TEM) foils were prepared within a Thermo Fisher Scientific dual-beam Helios UC G4 SEM/FIB. Secondary electron micrographs were captured with a 20 kV accelerating voltage and 30 µs dwell time, whereas foil lift outs were completed using a gallium ion beam following platinum deposition to protect the sample surfaces. HAADF scanning transmission electron microscopy (STEM) micrographs and STEM-EDS were captured using a Thermo Fisher Scientific Themis Z-STEM operating at 200 kV and equipped with an Ulti-Monochromator. Topographic AFM images were acquired via an Oxford Instruments Asylum Research Cypher system in AC tapping mode equipped with Budget Sensor Multi75E-G Cr/Pt coated probes (≈3 N m^{-1}, ≈75 kHz). Subsequent watershed analysis of AFM images was completed using Gwyddion 2.60 software.

High Temperature Multibeam Optical Stress Sensor Measurement (HT-MOSS): Temperature-dependent wafer curvature measurements were made within a HT-MOSS system comprising a furnace with optical access from the bottom.[76] An array of initially parallel laser beams was reflected off the film/substrate surface and into a charge coupled device (CCD). Curvatures were then obtained by measuring the divergence of these beams.[77] The relationship between film stress and substrate curvature is given by the Stoney equation,[40] which assumes that the film is much thinner than the substrate (the ratio of the film versus substrate thickness is roughly 1/2000 for the experiments reported here). During annealing, the furnace is maintained at 15 Torr with constant flow of N_2 (227 sccm).

Supporting Information

Supporting Information is available from the Wiley Online Library or from the author.

Acknowledgements

Initial HZO and TaN thin film synthesis, HTXRD, and ex situ wafer flexure measurements were supported by the Semiconductor Research Corporation's (SRC) Global Research Collaboration Program under task 2875.001. HZO film preparation, reactive ion etching, and atomic force microscopy measurements were supported by the Center for 3D Ferroelectric Microelectronics (3DFeM), an Energy Frontier Research Center funded by the U.S. Department of Energy, Office of Science, Basic Energy Sciences under Award No. DE-SC0021118. HT-MOSS measurements were supported by the National Science Foundation, under Award DMR-1832829. This research utilized a PHI VersaProbe III XPS system, which was supported by National Science Foundation Major Research Instrumentation Award #162601. This research utilized a Bruker D8 Diffractometer, which was supported by the National Science Foundation Award CHE-2018870. S.T.J. acknowledges support from the National Science Foundation Graduate Research Fellowship Program under award DGE-1842490. Sandia National Laboratories is a multimission laboratory managed and operated by National Technology and Engineering Solutions of Sandia, LLC, a wholly owned subsidiary of Honeywell International, Inc., for the U.S. Department

of Energy's National Nuclear Security Administration under contract DE-NA0003525. AFM experiments were conducted as part of a user project at the Center for Nanophase Materials Sciences, which is a US Department of Energy User Facility at Oak Ridge National Laboratory. This paper describes objective technical results and analysis. Any subjective views or opinions that might be expressed in the paper do not necessarily represent the views of the U.S. Department of Energy or the United States Government.

Conflict of Interest

The authors declare no conflict of interest.

Data Availability Statement

The data that support the findings of this study are available from the corresponding author upon reasonable request.

Keywords

biaxial stress, clamping effect, diffraction, ferroelectrics, hafnium zirconium oxide

Received: May 31, 2022
Revised: July 8, 2022
Published online: August 3, 2022

[1] J. Müller, T. S. Böscke, D. Bräuhaus, U. Schröder, U. Böttger, J. Sundqvist, P. Kücher, T. Mikolajick, L. Frey, *Appl. Phys. Lett.* **2011**, *99*, 112901.
[2] L. Chen, T.-Y. Wang, Y.-W. Dai, M.-Y. Cha, H. Zhu, Q.-Q. Sun, S.-J. Ding, P. Zhou, L. Chua, D. W. Zhang, *Nanoscale* **2018**, *10*, 15826.
[3] Y. Goh, S. Jeon, *Nanotechnology* **2018**, *29*, 335201.
[4] M. Hoffmann, B. Max, T. Mittmann, U. Schroeder, S. Slesazeck, T. Mikolajick, in *2018 IEEE Int. Electron Devices Meeting (IEDM)*, IEEE, Piscataway, NJ **2018**, pp. 31.6.1–31.6.4.
[5] M. Hoffmann, F. P. G. Fengler, M. Herzig, T. Mittmann, B. Max, U. Schroeder, R. Negrea, P. Lucian, S. Slesazeck, T. Mikolajick, *Nature* **2019**, *565*, 464.
[6] J. F. Ihlefeld, T. S. Luk, S. W. Smith, S. S. Fields, S. T. Jaszewski, W. T. Riffe, S. Bender, C. Constantin, M. V. Ayyasamy, P. V. Balachandran, P. Lu, M. D. Henry, P. S. Davids, *J. Appl. Phys.* **2020**, *128*, 034101.
[7] S. W. Smith, A. R. Kitahara, M. A. Rodriguez, M. D. Henry, M. T. Brumbach, J. F. Ihlefeld, *Appl. Phys. Lett.* **2017**, *110*, 072901.
[8] S. W. Smith, M. D. Henry, M. T. Brumbach, M. A. Rodriguez, J. F. Ihlefeld, *Appl. Phys. Lett.* **2018**, *113*, 182904.
[9] T. S. Böscke, J. Müller, D. Bräuhaus, U. Schröder, U. Böttger, *Appl. Phys. Lett.* **2011**, *99*, 102903.
[10] R. Batra, T. D. Huan, J. L. Jones, G. Rossetti, R. Ramprasad, *J. Phys. Chem. C* **2017**, *121*, 4139.
[11] X. Sang, E. D. Grimley, T. Schenk, U. Schroeder, J. M. LeBeau, *Appl. Phys. Lett.* **2015**, *106*, 162905.
[12] A. K. Saha, K. Ni, S. Dutta, S. Datta, S. Gupta, *Appl. Phys. Lett.* **2019**, *114*, 202903.
[13] C. Künneth, R. Materlik, A. Kersch, *J. Appl. Phys.* **2017**, *121*, 205304.
[14] H. J. Kim, M. H. Park, Y. J. Kim, Y. H. Lee, W. Jeon, T. Gwon, T. Moon, K. D. Kim, C. S. Hwang, *Appl. Phys. Lett.* **2014**, *105*, 192903.
[15] U. Schroeder, C. Richter, M. H. Park, T. Schenk, M. Pešić, M. Hoffmann, F. P. G. Fengler, D. Pohl, B. Rellinghaus, C. Zhou, C.-C. Chung, J. L. Jones, T. Mikolajick, *Inorg. Chem.* **2018**, *57*, 2752.
[16] J. Müller, U. Schröder, T. S. Böscke, I. Müller, U. Böttger, L. Wilde, J. Sundqvist, M. Lemberger, P. Kücher, T. Mikolajick, L. Frey, *J. Appl. Phys.* **2011**, *110*, 114113.
[17] J. Müller, T. S. Böscke, U. Schröder, S. Mueller, D. Bräuhaus, U. Böttger, L. Frey, T. Mikolajick, *Nano Lett.* **2012**, *12*, 4318.
[18] T. Shiraishi, K. Katayama, T. Yokouchi, T. Shimizu, T. Oikawa, O. Sakata, H. Uchida, Y. Imai, T. Kiguchi, T. J. Konno, H. Funakubo, *Appl. Phys. Lett.* **2016**, *108*, 262904.
[19] T. Shiraishi, K. Katayama, T. Yokouchi, T. Shimizu, T. Oikawa, O. Sakata, H. Uchida, Y. Imai, T. Kiguchi, T. J. Konno, H. Funakubo, *Mater. Sci. Semicond. Process.* **2017**, *70*, 239.
[20] A. Pal, V. K. Narasimhan, S. Weeks, K. Littau, D. Pramanik, T. Chiang, *Appl. Phys. Lett.* **2017**, *110*, 022903.
[21] D. R. Islamov, T. M. Zalyalov, O. M. Orlov, V. A. Gritsenko, G. Ya Krasnikov, *Appl. Phys. Lett.* **2020**, *117*, 162901.
[22] M. Hoffmann, U. Schroeder, T. Schenk, T. Shimizu, H. Funakubo, O. Sakata, D. Pohl, M. Drescher, C. Adelmann, R. Materlik, A. Kersch, T. Mikolajick, *J. Appl. Phys.* **2015**, *118*, 072006.
[23] E. A. Scott, S. W. Smith, M. D. Henry, C. M. Rost, A. Giri, J. T. Gaskins, S. S. Fields, S. T. Jaszewski, J. F. Ihlefeld, P. E. Hopkins, *Appl. Phys. Lett.* **2018**, *113*, 192901.
[24] S. S. Cheema, D. Kwon, N. Shanker, R. dos Reis, S.-L. Hsu, J. Xiao, H. Zhang, R. Wagner, A. Datar, M. R. McCarter, C. R. Serrao, A. K. Yadav, G. Karbasian, C.-H. Hsu, A. J. Tan, L.-C. Wang, V. Thakare, X. Zhang, A. Mehta, E. Karapetrova, R. V. Chopdekar, P. Shafer, E. Arenholz, C. Hu, R. Proksch, R. Ramesh, J. Ciston, S. Salahuddin, *Nature* **2020**, *580*, 478.
[25] K. J. Hubbard, D. G. Schlom, *J. Mater. Res.* **1996**, *11*, 2757.
[26] D. G. Schlom, S. Guha, S. Datta, *MRS Bull.* **2008**, *33*, 1017.
[27] P. Polakowski, J. Müller, *Appl. Phys. Lett.* **2015**, *106*, 232905.
[28] A. Chernikova, *Microelectron. Eng.* **2015**, *147*, 15.
[29] T. Nishimura, L. Xu, S. Shibayama, T. Yajima, S. Migita, A. Toriumi, *Jpn. J. Appl. Phys.* **2016**, *55*, 08PB01.
[30] T. S. Böscke, St. Teichert, D. Bräuhaus, J. Müller, U. Schröder, U. Böttger, T. Mikolajick, *Appl. Phys. Lett.* **2011**, *99*, 112904.
[31] S. Starschich, D. Griesche, T. Schneller, U. Böttger, *ECS J. Solid State Sci. Technol.* **2015**, *4*, P419.
[32] S. Migita, H. Ota, K. Shibuya, H. Yamada, A. Sawa, T. Matsukawa, A. Toriumi, *Jpn. J. Appl. Phys.* **2019**, *58*, SBBA07.
[33] S. J. Kim, D. Narayan, J.-G. Lee, J. Mohan, J. S. Lee, J. Lee, H. S. Kim, Y.-C. Byun, A. T. Lucero, C. D. Young, S. R. Summerfelt, T. San, L. Colombo, J. Kim, *Appl. Phys. Lett.* **2017**, *111*, 242901.
[34] S. Mueller, J. Mueller, A. Singh, S. Riedel, J. Sundqvist, U. Schroeder, T. Mikolajick, *Adv. Funct. Mater.* **2012**, *22*, 2412.
[35] R. Materlik, C. Künneth, A. Kersch, *J. Appl. Phys.* **2015**, *117*, 134109.
[36] Personal Communication with Professor Andrew Rappe.
[37] S. J. Kim, J. Mohan, H. S. Kim, J. Lee, C. D. Young, L. Colombo, S. R. Summerfelt, T. San, J. Kim, *Appl. Phys. Lett.* **2018**, *113*, 182903.
[38] T. Schenk, C. M. Fancher, M. H. Park, C. Richter, C. Künneth, A. Kersch, J. L. Jones, T. Mikolajick, U. Schroeder, *Adv. Electron. Mater.* **2019**, *5*, 1900303.
[39] C. H. Hsueh, C. R. Luttrell, T. Cui, *J. Micromech. Microeng.* **2006**, *16*, 2509.
[40] B. Freund, S. Suresh, *Thin Film Materials; Stress, Defect Formation, and Surface Evolution*, Cambridge University Press, New York **2006**.
[41] D. H. Triyoso, P. J. Tobin, B. E. White, R. Gregory, X. D. Wang, *Appl. Phys. Lett.* **2006**, *89*, 132903.
[42] M. H. Park, Y. H. Lee, H. J. Kim, T. Schenk, W. Lee, K. D. Kim, F. P. G. Fengler, T. Mikolajick, U. Schroeder, C. S. Hwang, *Nanoscale* **2017**, *9*, 9973.
[43] M. Lederer, T. Kämpfe, R. Olivo, D. Lehninger, C. Mart, S. Kirbach, T. Ali, P. Polakowski, L. Roy, K. Seidel, *Appl. Phys. Lett.* **2019**, *115*, 222902.

[44] T. Mittmann, M. Materano, P. D. Lomenzo, M. H. Park, I. Stolichnov, M. Cavalieri, C. Zhou, C.-C. Chung, J. L. Jones, T. Szyjka, M. Müller, A. Kersch, T. Mikolajick, U. Schroeder, *Adv. Mater. Interfaces* **2019**, *6*, 1900042.
[45] L. Baumgarten, T. Szyjka, T. Mittmann, M. Materano, Y. Matveyev, C. Schlueter, T. Mikolajick, U. Schroeder, M. Müller, *Appl. Phys. Lett.* **2021**, *118*, 032903.
[46] Y. H. Lee, H. J. Kim, T. Moon, K. D. Kim, S. D. Hyun, H. W. Park, Y. B. Lee, M. H. Park, C. S. Hwang, *Nanotechnology* **2017**, *28*, 305703.
[47] S. S. Fields, S. W. Smith, C. M. Fancher, M. D. Henry, S. L. Wolfley, M. G. Sales, S. T. Jaszewski, M. A. Rodriguez, G. Esteves, P. S. Davids, S. J. McDonnell, J. F. Ihlefeld, *Adv. Mater. Interfaces* **2021**, *8*, 2100018.
[48] W. Hamouda, A. Pancotti, C. Lubin, L. Tortech, C. Richter, T. Mikolajick, U. Schroeder, N. Barrett, *J. Appl. Phys.* **2020**, *127*, 064105.
[49] W. Hamouda, C. Lubin, S. Ueda, Y. Yamashita, O. Renault, F. Mehmood, T. Mikolajick, U. Schroeder, R. Negrea, N. Barrett, *Appl. Phys. Lett.* **2020**, *116*, 252903.
[50] F. P. G. Fengler, M. Pešić, S. Starschich, T. Schneller, C. Künneth, U. Böttger, H. Mulaosmanovic, T. Schenk, M. H. Park, R. Nigon, P. Muralt, T. Mikolajick, U. Schroeder, *Adv. Electron. Mater.* **2017**, *3*, 1600505.
[51] A. Chouprik, M. Spiridonov, S. Zarubin, R. Kirtaev, V. Mikheev, Y. Lebedinskii, S. Zakharchenko, D. Negrov, *ACS Appl. Electron. Mater.* **2019**, *1*, 275.
[52] E. D. Grimley, T. Schenk, X. Sang, M. Pešić, U. Schroeder, T. Mikolajick, J. M. LeBeau, *Adv. Electron. Mater.* **2016**, *2*, 1600173.
[53] S. S. Fields, S. W. Smith, P. J. Ryan, S. T. Jaszewski, I. A. Brummel, A. Salanova, G. Esteves, S. L. Wolfley, M. D. Henry, P. S. Davids, J. F. Ihlefeld, *ACS Appl. Mater. Interfaces* **2020**, *12*, 26577.
[54] T. Schenk, M. Hoffmann, J. Ocker, M. Pešić, T. Mikolajick, U. Schroeder, *ACS Appl. Mater. Interfaces* **2015**, *7*, 20224.
[55] Y. Goh, S. Jeon, *J. Vac. Sci. Technol. B* **2018**, *36*, 052204.
[56] M. Hoffmann, T. Schenk, M. Pešić, U. Schroeder, T. Mikolajick, *Appl. Phys. Lett.* **2017**, *111*, 182902.
[57] S. S. Fields, D. H. Olson, S. T. Jaszewski, C. M. Fancher, S. W. Smith, D. A. Dickie, G. Esteves, M. D. Henry, P. S. Davids, P. E. Hopkins, J. F. Ihlefeld, *Appl. Phys. Lett.* **2021**, *118*, 102901.
[58] S. S. Fields, S. W. Smith, S. T. Jaszewski, T. Mimura, D. A. Dickie, G. Esteves, M. David Henry, S. L. Wolfley, P. S. Davids, J. F. Ihlefeld, *J. Appl. Phys.* **2021**, *130*, 134101.
[59] S. Zafar, H. Jagannathan, L. F. Edge, D. Gupta, *Appl. Phys. Lett.* **2011**, *98*, 152903.
[60] K. Park, D. R. Olander, *J. Electrochem. Soc.* **1991**, *138*, 1154.
[61] F. Huang, X. Chen, X. Liang, J. Qin, Y. Zhang, T. Huang, Z. Wang, B. Peng, P. Zhou, H. Lu, L. Zhang, L. Deng, M. Liu, Q. Liu, H. Tian, L. Bi, *Phys. Chem. Chem. Phys.* **2017**, *19*, 3486.
[62] D. R. Islamov, T. V. Perevalov, V. A. Gritsenko, C. H. Cheng, A. Chin, *Appl. Phys. Lett.* **2015**, *106*, 102906.
[63] D. R. Islamov, V. A. Gritsenko, T. V. Perevalov, V. A. Pustovarov, O. M. Orlov, A. G. Chernikova, A. M. Markeev, S. Slesazeck, U. Schroeder, T. Mikolajick, G. Y. Krasnikov, *Acta Mater.* **2019**, *166*, 47.
[64] Standard Test Methods for Determining Average Grain Size, ASTM International, https://www.astm.org/e0112-10.html (accessed: December 2021).
[65] M. H. Park, C.-C. Chung, T. Schenk, C. Richter, K. Opsomer, C. Detavernier, C. Adelmann, J. L. Jones, T. Mikolajick, U. Schroeder, *Adv. Electron. Mater.* **2018**, *4*, 1800091.
[66] S.-T. Fan, Y.-W. Chen, C. W. Liu, *J. Phys. D: Appl. Phys.* **2020**, *53*, 23LT01.
[67] M. Birkholz, *Thin Film Analysis by X-Ray Scattering*, Wiley VCH, Weinheim **2006**.
[68] S. L. Dole, O. Hunter, C. J. Wooge, *J. Am. Ceram. Soc.* **1977**, *60*, 488.
[69] X.-S. Zhao, S.-L. Shang, Z.-K. Liu, J.-Y. Shen, *J. Nucl. Mater.* **2011**, *415*, 13.
[70] A. SelCuk, A. Atkinson, *J. Eur. Ceram. Soc.* **1997**, *17*, 1523.
[71] J. J. Wortman, R. A. Evans, *J. Appl. Phys.* **1965**, *36*, 153.
[72] Y. Goh, J. Hwang, Y. Lee, M. Kim, S. Jeon, *Appl. Phys. Lett.* **2020**, *117*, 242901.
[73] J. Kieffer, V. Valls, N. Blanc, C. Hennig, *J. Synchrotron Radiat.* **2020**, *27*, 558.
[74] G. Esteves, K. Ramos, C. M. Fancher, J. L. Jones, *LIPRAS: Line-Profile Analysis Software*, North Carolina State University, Raleigh, North Carolina.
[75] B. H. Toby, R. B. Von Dreele, *J. Appl. Crystallogr.* **2013**, *46*, 544.
[76] S. Bhatia, B. W. Sheldon, *J. Am. Ceram. Soc.* **2008**, *91*, 3986.
[77] J. A. Floro, E. Chason, R. D. Twesten, R. Q. Hwang, L. B. Freund, *Phys. Rev. Lett.* **1997**, *79*, 3946.